

Vibrational Spectra of $\text{Pb}_2\text{Bi}_2\text{Te}_3$, PbBi_2Te_4 and PbBi_4Te_7 Topological Insulators: Temperature Dependent Raman and Theoretical Insight from DFT Simulations

Priyanath Mal^a, Ganesh Bera^a, G. R. Turpu^a, Sunil. K. Srivastava^b, A. Gangan^c,
Brahmananda Chakraborty^{*c}, Bipul Das^d and Pradip Das^{†a}

^aDepartment of Pure and Applied Physics, Guru Ghasidas Vishwavidyalaya, Koni, Bilaspur-495009, India.

^bDepartment of Physics, Mahatma Gandhi Central University, East Champaran, Motihari, Bihar-845401, India.

^cHigh Pressure and Synchrotron Radiation Physics Division, Bhabha Atomic Research Center, Trombay, Mumbai-40008, India.

^dNational Changhua University of Education, Jin-De Road, Changhua 500, Taiwan.

Abstract

We present temperature dependent frequency shift and line broadening of phonon modes by insertion of atomic layers of Pb and PbTe in the prototype 3D topological insulator Bi_2Te_3 , using Raman spectroscopy. Good quality single crystals of $\text{Pb}_2\text{Bi}_2\text{Te}_3$, PbBi_2Te_4 and PbBi_4Te_7 are grown using the modified Bridgman technique. The Raman modes show progressive blue shift with the decrease in temperature from 298 K to 93 K in $\text{Pb}_2\text{Bi}_2\text{Te}_3$, PbBi_2Te_4 and PbBi_4Te_7 is due to anharmonic vibrations of the lattice as well as increasing strength of Bi-Te covalent interactions. Experimental results are complemented by extensive density functional theory calculations where a reasonable matching between experimental and computational data is found. Chemical pressure, induces by the insertion of Pb and PbTe layers in Bi_2Te_3 , modifies the interactions at the boundaries of the quintuple-layers which is evident from the evolution of A_{1u}^2 mode. The enhancement of out-of-plane Bi-Te vibrations with respect to in-plane Bi-Te vibrations are observed at low temperatures.

Introduction

Topological insulators (TIs) are materials that behave as insulators in its interior, but always have conducting boundaries. This compelling characteristic of topological insulator is possible due to strong spin orbit coupling (SOC) of heavy elements, which constitute the topological insulators. [1, 2, 3] Furthermore, the topological order is protected by time reversal symmetry analogous to the quantum spin Hall effect.[1, 2, 3, 4] The potential applications of TIs in spintronic [5], quantum computing and low power electronics [1, 2] etc. bring it into the spot light of research over the last decade. Considerable amount of research efforts have been devoted to understand the layered structures, e.g. Bi_2Te_3 , PbBi_2Te_4 and PbBi_4Te_7 due to their unique and interesting bulk thermo-electric properties [6, 7, 8, 9] and topological surface states. [10, 11, 12, 13] It is crucial to understand the phonon-phonon and electron-phonon interactions in these layered materials, in order to use these fascinating materials for practical use. Recently, phonon confinement effect is identified through Raman scattering below three quintuple-layers (QLs) for Bi_2Te_3 by Wang *et al.* [14] Most studied Bi_2Se_3 , categorically in the $\text{B(V)}_2\text{A(VI)}_3$ group possesses D_{3d}^5 point group symmetry having fifteen different bulk phonon modes at Γ point and the irreducible representations can be expressed as: $\Gamma_{\text{bulk}} = 2(\text{A}_{1g} + \text{E}_g) + 3(\text{E}_u + \text{A}_{2u})$. [15] The odd and even parity phonons are related to Raman and IR active modes of lattice vibrations respectively, of the bulk Bi_2Te_3 like materials with inversion symmetry in the crystal structure. [16] Out of fifteen phonon modes, three (E_u) are acoustic modes and another twelve are optical in which, $2(\text{E}_g + \text{A}_{1g})$ are Raman active in the range $20\text{-}200\text{ cm}^{-1}$. [15] The Raman active E_g modes are related to in-plane A(VI)-B(V) and that of A_{1u} corresponds to out-of-plane IR lattice vibrations. [17] Cheng *et al.* [18] predict A_{1g} and A_{1u} modes

are affected by the van-der-Waals interactions present in between QLs of layered Bi_2Te_3 and independent of spin orbit coupling. The modes E_g and E_u both have nearly the same frequency split due to the van-der-Waals interactions.[18] Although the room temperature (RT) and low temperature Raman characterizations of the prototype Bi_2Se_3 and Bi_2Te_3 TIs are available in literature, but little attention has been paid to Pb based TIs such as PbBi_2Te_4 and PbBi_4Te_7 at room temperature as well as at low temperatures. Topological phenomenon has also been reported in $\text{Bi}_2/\text{Bi}_2\text{Te}_3$ heterostructure.[19] Bi_4Te_3 has same structure as that of hetero structure is one of the member among seven different room temperature phases of Bi_xTe_y . [20, 21] Lind *et al.*[22] have theoretically predicted that the insertion of Bi_2 layers periodically in the van-der-Waals gaps of Bi_2Se_3 closes the bulk energy gap of Bi_2Se_3 converts it into a semimetal. Valla *et al.*[23] have explored the existence of topologically protected surface states at the Γ point in the single crystal samples of $\text{Bi}_4\text{Se}_{2.6}\text{S}_{0.4}$ and found $\text{Bi}_4\text{Se}_{2.6}\text{S}_{0.4}$ as topological semimetal. Many issues are related [20, 24] to the vibrational properties of $(\text{Bi}_2)(\text{Bi}_2\text{Te}_3)$ have not yet received desire amount of attention, motivate us to investigate the vibrational properties of intermetallic $(\text{Pb}_2)(\text{Bi}_2\text{Te}_3)$ single crystal for better understanding of these isostructural compounds, where the topological behavior by angle resolve photoemission spectroscopy (ARPES) is yet to set.

Here we provide a systematic investigation of the synthesis and temperature dependent Raman studies of Bi_2Te_3 , $\text{Pb}_2\text{Bi}_2\text{Te}_3$, PbBi_2Te_4 and PbBi_4Te_7 high quality single crystals in the temperature range of 93 K to 298 K. The observed blue shift in the Raman modes is explained in terms of anharmonic lattice vibrations of Bi_2Te_3 and $\text{Pb}_2\text{Bi}_2\text{Te}_3$ and or by increasing stiffness of Bi-Te interactions for PbBi_2Te_4 and PbBi_4Te_7 at lower temperature. The chemical pressure induces by intercalation results in observation of out-of-plane Bi-Te

vibrations at $\sim 132\text{ cm}^{-1}$ for $\text{Pb}_2\text{Bi}_2\text{Te}_3$ and PbBi_2Te_4 . The observed modes of all the samples are theoretically verified through density functional theory (DFT) calculations.

Experimental

High quality single crystals of binary Bi_2Te_3 , ternary $\text{Pb}_2\text{Bi}_2\text{Te}_3$, PbBi_2Te_4 and PbBi_4Te_7 layered chalcogenides are synthesized by reacting homogeneously mixed powder of Bi (Alfa Aesar), Pb (Sigma-Aldrich) and Te (Sigma-Aldrich) of analytical grade in a sealed evacuated quartz tube with conical tip, flashing frequently with Ar. The ampoules are then heat treated to $\sim 1223\text{ K}$ for 24 hrs. and are cooled it down to $\sim 893\text{ K}$ in an ~ 6 days followed by furnace cooling to room temperature. During the growth, to avoid multi-nucleation the ampoules are kept in pointed bottom configuration, resulting in the growth of the ingots of suitable length with different large crystalline faces. The crystallinity of the samples are investigated at RT by using Rigaku x-ray diffractometer, operating at 3 kW, equipped with Cu-K α radiation in the 2θ angular range of 10° to 90° with a step size of 0.01° . The chemical homogeneity of the prepared single crystals is then confirmed through SEM-EDAX analysis. Temperature dependent Raman spectra are then recorded in the basal plane of a back scattering geometry for the same crystalline faces of different specimens in the range of 298 K to 93 K with Technos STR-500 micro-Raman spectrometer equipped with 532 nm diode laser source with a spectral resolution of 1 cm^{-1} . The sample stage from Linkam THMS600 facilitated with temperature controller is used to control the sample temperature at desired value in each step of the temperature dependent Raman (TDR) measurement. During the Raman measurement the laser power is kept $< 2\text{ mW}$ in order to avoid surface burning and oxidation.

Results and discussion

As grown silver color platelet crystals are easily cleaved off from the ingots. For polycrystalline x-ray powder diffraction, small pieces of crystalline blocks from different parts, along the length of ingot for different compounds, are crushed into respective powder and are recorded in the Bragg-Brentano configuration at room temperature. The Rietveld refinements of the RT powder patterns of respective chalcogenides are illustrated in [Fig. 1\(a\)](#). The calculated patterns (continuous black lines) are matched well with the observed profiles (red solid lines) and absence of any parasitic peaks establishes phase purity of different single crystals. Pseudo-Voigt function and linear interpolation as implemented in FullProf Suite program (2.05), version: July-2011[25] are used for defining the peak shapes and pattern backgrounds respectively. The growth direction of the mechanically exfoliate shiny crystalline faces having thicknesses of $\sim 135 \mu\text{m}$ for Bi_2Te_3 , $\sim 61 \mu\text{m}$ for $\text{Pb}_2\text{Bi}_2\text{Te}_3$, $\sim 151 \mu\text{m}$ for PbBi_2Te_4 and $\sim 105 \mu\text{m}$ for PbBi_4Te_7 are investigated (for more information about thickness measurement see [Fig. S1 in supplementary](#)). The good crystallinity in all the samples is proved by their sharp c axes ($00l$) Bragg reflections in their respective x-ray diffraction patterns and are illustrated in [Fig. 1\(b\)](#).

Refined lattice parameters and Wyckoff positions are modelled by VESTA 3.1.8, electronic and structural analysis software package [26] and are illustrated in [Fig. 2\(a-d\)](#). The structural refinement suggests that, the layered rhombohedral structure with space group R-3m (166) for bulk Bi_2Te_3 , $\text{Pb}_2\text{Bi}_2\text{Te}_3$ and PbBi_2Te_4 ; whereas PbBi_4Te_7 belongs to P-3m1 (164). With nearly same lattice parameter $a = 4.461 \text{ \AA}$, the unit cell of bulk $\text{Pb}_2\text{Bi}_2\text{Te}_3$ [$(\text{Pb}_2)(\text{Bi}_2\text{Te}_3)$] contains three bilayers of Pb and three Bi_2Te_3 QLs, which are alternately arranged along the crystallographic c axis in the sequence: $-(\text{Te}(2)\text{-Bi}\text{-Te}(1)\text{-Bi}\text{-Te}(2))\text{-(Pb-Pb)-}$; leads to elongation of

c axis from ~ 30.702 Å for Bi_2Te_3 to ~ 41.947 Å. Covalent interactions between the $6p$ orbitals of Pb atoms in the Pb bilayers make the slab stable. PbBi_2Te_4 $[(\text{PbTe})(\text{Bi}_2\text{Te}_3)]$ unit cell consists of three seven-layers packets: $-(\text{Te}(2)\text{-Bi-Te}(1)\text{-Pb-Te}(1)\text{-Bi-Te}(2))$ - i.e. the seven monoatomic layers are centro-symmetrical with reference to Pb; Pb acts as inversion center. The insertion of PbTe layers in Bi_2Te_3 QLs leads to the elongation of c axis (~ 42.003 Å). Five atomic layers of Bi_2Te_3 block are separated from PbBi_2Te_4 block by van-der-Waals gaps in the hexagonal unit cell of PbBi_4Te_7 , consists of a total twelve atomic layers arranged periodically along the crystallographic c axis that eventually leads to the evolution of three dimensional crystal structure.

In order to investigate the modifications of lattice vibrations and phonon dynamics of $\text{Pb}_2\text{Bi}_2\text{Te}_3$, PbBi_2Te_4 and PbBi_4Te_7 caused by the insertion of Pb and PbTe layers in Bi_2Te_3 in the temperature range from RT to ~ 93 K, we start with the virgin Bi_2Te_3 . At room temperature, four phonon modes at 94, 104, 124 and 142 cm^{-1} respectively have been identified and are illustrated in Fig. 3(a). The 104 cm^{-1} i.e., E_g^2 mode and 142 cm^{-1} i.e., A_{1g}^2 mode are related to the in-plane and the out-of-plane Bi, Te vibrations respectively. The 124 cm^{-1} i.e., A_{1u}^1 mode is IR active in bulk and corresponds to the out-of-plane vibrations of the Bi, Te atoms.[17] [Teweldebrhan et al.\[27\]](#) have observed 120 cm^{-1} mode and described it as symmetry breaking in atomically thin films of Bi_2Te_3 . Blue shift is observed for all the modes in the temperature range from RT to 93 K. The evaluation of out-of-plane A_{1u}^1 and A_{1g}^2 modes relative to the in-plane E_g^2 mode with decreasing temperature signify the reduction of strain and reinforcement of the out-of-plane Bi-Te vibrations relative to the in-plane motion. The inset in Fig. 3(a) has illustrated the Lorentzian line shape fitting for the observed modes at 93 K. Fig.

4(a) has illustrated the linear fit of temperature variation of the A_{1g}^2 mode having with a slope of $0.01264 \pm 0.00083 \text{ cm}^{-1}\text{K}^{-1}$ which is in good agreement with [Park *et al.*\[28\]](#)

[Fig. 3\(b\)](#) has illustrated the temperature dependent Raman spectra for $\text{Pb}_2\text{Bi}_2\text{Te}_3$. At room temperature we have identified Raman modes at 94, 104 and 124 cm^{-1} respectively along with a notch at 142 cm^{-1} . The mode at 124 cm^{-1} is relatively broad; multi-peaks fit by considering Lorentzian line shape shows the existence of two distinct modes at $\sim 124 \text{ cm}^{-1}$ i.e., A_{1u}^1 and $\sim 132 \text{ cm}^{-1}$ i.e., A_{1u}^2 respectively. With lowering the temperature these two modes become completely distinct at $\sim 183 \text{ K}$. This observation can be explained by considering thermal noise effect which get suppress with decreasing temperature from RT and finally at low temperature, the phonon scattering effect becomes insignificant, makes the modes prominent and distinct. The notch like 142 cm^{-1} i.e., A_{1g}^2 mode evolves to a shape of peak at $\sim 263 \text{ K}$ and after that its intensity changes gradually till the end of the temperature variation (i.e., lowest temperature achieved) and are illustrated in the main panel of the [Fig. 3\(b\)](#). At 93 K the modes appear at 94, 106, 126, 137 and 145 cm^{-1} respectively. Theoretically predicted A_{1u}^2 mode for Bi_2Te_3 is identified distinctly at $\sim 137 \text{ cm}^{-1}$ for $\text{Pb}_2\text{Bi}_2\text{Te}_3$ at low temperature. [Xu *et al.* \[20\]](#) have identified a very negligible signature of 132 cm^{-1} mode and explained as weak bonding effects at the boundaries of QLs. In our case, the A_{1u}^2 mode at room temperature is very hard to observe but with decreasing temperature this becomes distinct. It can be justified by considering the chemical pressure as induces by Pb layers insertion in Bi_2Te_3 QLs and results in increasing strength of interactions at the boundaries of Pb layers and Bi_2Te_3 QL slabs. It is to be noted that,

simultaneously the strength of out-of-plane Bi-Te vibrations increases with decreasing the temperature from RT. These two combined effects can be attributed to the evolution of A_{1u}^2 mode. For both Bi_2Te_3 and $\text{Pb}_2\text{Bi}_2\text{Te}_3$ the E_g^2 mode appears at 104 cm^{-1} infers that the nature of covalent interactions and corresponding in-plane motion of Bi-Te are same for both crystals. At RT, the 104 cm^{-1} mode takes the highest value, but as we go down the temperature to 93 K , the 124 cm^{-1} peak evolves gradually and becomes the highest intense mode at $\sim 93 \text{ K}$ reflects the fact that the out-of-plane Bi-Te vibrations become less restrain over the in-plane Bi-Te vibrations at low temperatures.

Now we focus our attention on the PbBi_2Te_4 Raman modes at $95, 105, 142 \text{ cm}^{-1}$ and two small humps at 124 and 131 cm^{-1} respectively that are observed at room temperature are illustrated clearly in Fig. 3(c). The exact peak positions for these two humps are obtained by deconvoluting the spectra using Lorentzian function. The shapes of the humps gradually evolve at the cost of lowering the temperature and become distinct at $\sim 183 \text{ K}$. In total, we have identified five modes at low temperature. The intensity of E_g^2 mode at 105 cm^{-1} decrease gradually relative to the A_{1u}^1 mode at 124 cm^{-1} as we decreases the temperature and A_{1u}^1 becomes the highest one at 93 K . The evolution of humps and increasing intensity of A_{1u}^1 relative to E_g^2 establish the enhancement of out-of-plane Bi-Te vibrations compare to in-plane Bi-Te vibrations at low temperatures. The existence of the 131 cm^{-1} i.e., A_{1u}^2 mode may indicate the modification of the van-der-Waals interactions at the boundaries of QLs. The E_g^2 mode for PbBi_2Te_4 arises at 105 cm^{-1} but for Bi_2Te_3 and $\text{Pb}_2\text{Bi}_2\text{Te}_3$, the peak position is same ($\sim 104 \text{ cm}^{-1}$). It indicates that, the insertion

of PbTe atomic layers in Bi_2Te_3 slightly modify the covalent interactions between Bi-Te as the Pb atom is at the centro-symmetrical position and is connected with the Te atom and another end of Te is connected with the Bi. Thus Pb in turn modifies the covalent interactions in Bi-Te atoms pair.

[Fig. 3\(d\)](#) has illustrated the temperature variation of Raman modes of PbBi_4Te_7 . Two distinct modes E_g^2 at 104 cm^{-1} and A_{1u}^1 at 124 cm^{-1} are identified at RT. With decreasing temperature the A_{1u}^1 mode evolves gradually and its intensity becomes almost equal to E_g^2 at $\sim 163\text{ K}$. A new mode is observed at $\sim 147\text{ cm}^{-1}$ at $\sim 113\text{ K}$ and becomes distinct at the lowest measure temperature here, which can be explained in terms of the enhancement of the out-of-plane vibrations over in-plane Bi-Te vibrations at lower temperatures. The maturity of A_{1g}^2 mode at 142 cm^{-1} is accompanied by the enhancement of the A_{1u}^1 mode which becomes the most intense Raman mode at $\sim 113\text{ K}$. Due to poor signal to noise ratio the spectra observed in case of PbBi_4Te_7 , the mode at $\sim 95\text{ cm}^{-1}$ is not well resolved and the appearance of new mode at 147 cm^{-1} due to insertion of PbTe layers is not clearly visible, therefore only three modes at 111 , ~ 130 and 147 cm^{-1} are discussed here.

The observed $\sim 95\text{ cm}^{-1}$ mode for Bi_2Te_3 , $\text{Pb}_2\text{Bi}_2\text{Te}_3$ and PbBi_2Te_4 more or less behaves in the same way. That means, with lowering the temperature; they remain un-shifted but their shapes evolve gradually and are broadened as clearly observed in the [Fig. 3\(a-c\)](#). This is in good agreement with the [Wang *et al.*\[14\]](#), who have performed their experiment on MBE grown thin film and Raman measurement under ultra-high vacuum, explains 95 cm^{-1} mode as the surface phonon mode. But the origin of this mode is not beyond debate, [He *et al.*\[29\]](#) have argued that, the inversion symmetry breaking for their nano-plates whereas, [Jian-Hua *et al.*\[30\]](#)

have described it as surface oxidation effect. Very recently [Fernández *et al.*\[31\]](#) reports that, Te clusters in Te rich Bi_2Te_3 leads to 88 cm^{-1} mode. We have found 95 cm^{-1} mode in theoretical studies in DFT calculation.

The peak position and full width half maxima (FWHM) as obtain from Lorentzian line shape fitting of individual modes as a function of temperature for each specimen are illustrated in [Fig. 4\(a-d\)](#). Temperature dependency of peak positions for the observed Bi_2Te_3 and $\text{Pb}_2\text{Bi}_2\text{Te}_3$ Raman modes are fitted well with the consideration of anharmonic phonon-phonon coupling along with thermal expansion.[\[28\]](#) It provides a reasonably precise depiction of the phonon temperature dependence in some semiconductors and diamond.[\[32, 33\]](#) Let, ω_0 is the bare harmonic frequency, χ'/T is due to the lattice thermal expansion, and χ''/T^2 is the anharmonic phonon-phonon coupling term. Therefore, the temperature dependence of the phonon frequency can be given by:

$$\omega = \omega_0 + \chi'/T + \chi''/T^2,$$

where χ' and χ'' are first order and second order temperature coefficients respectively. For PbBi_2Te_4 and PbBi_4Te_7 with decreasing the temperature from RT, the modes shift towards the higher wave number side. It infers that, the strength of covalent interactions between Bi-Te increases and hence force constant of the interacting forces increase which in turn produces blue shift in Raman modes. As a result of insertion of Pb and PbTe layers in Bi_2Te_3 the out-of-plane Bi-Te vibrations become less restrained compare to the in-plane vibrations as temperature decreases from RT to 93 K. Increase of slope of the A_{1g}^2 mode is tabulated in

[Table 1.](#)

Density functional theory simulations

We have also performed First principles simulations and computed the Raman modes and frequencies for all the samples. All the calculations have been performed within the framework of density functional theory using the Quantum espresso 5.3.0 code.[34] We have used the tested PBEsol pseudo potential for Bi, Pb and Te from THOES library.[35] The plane waves and charge density cut-off is set to 55 Ry and 500 Ry respectively and a Monkhorst-Pack [36] grid of k -points is chosen according to the symmetry of the crystal. The phonon properties are calculated using the phonopy package [37] which is used for post-processing the data from Quantum espresso. A super-cell and finite difference (FD) approach are used to calculate the dynamical matrix. Fig. 5(a-c) represents the density of states (DOS) plots for $\text{Pb}_2\text{Bi}_2\text{Te}_3$, PbBi_2Te_4 and PbBi_4Te_7 respectively. The electronic properties as display in Fig. 5(a-c) reveal that PbBi_2Te_4 and PbBi_4Te_7 exhibit insulating character whereas $\text{Pb}_2\text{Bi}_2\text{Te}_3$ possesses semi-metallic signature. $\text{Pb}_2\text{Bi}_2\text{Te}_3$ is analogous to Bi_4Te_3 , which is reported to be semi metallic.[21] So it is expected that $\text{Pb}_2\text{Bi}_2\text{Te}_3$ may behave as semi-metallic. We can infer that due to the insertion of Pb slab within the Bi_2Te_3 slabs the narrow gap (~ 170 meV) of Bi_2Te_3 vanishes and system becomes metallic, this finding is consistent with literature report.[22] The experimentally observed Raman modes and the frequencies for the bulk structures of PbBi_2Te_4 , PbBi_4Te_7 are the same as that obtained from bulk Bi_2Te_3 . The main reason is the higher atomic weight of the Pb atom which reduces the mode frequency under harmonic approximations (since, $\omega = \sqrt{k/M}$), which is clearly seen from the PPDOS and are illustrated in Fig. 6(a-c). The phonon modes from Pb only contribute to the lower side of the spectrum and not of those which are a Raman signature. Theoretically calculated mode frequencies along with the experimentally observed frequencies are tabulated in Table 2. For bulk PbBi_2Te_4 ,

Raman modes match nicely with the experimental observations except slight deviation for low frequency modes. The low frequency mode at $\sim 95 \text{ cm}^{-1}$ obtained in experiment comes at little lower frequency (81 cm^{-1}). This deviation between experiment and theory is very much reasonable as Cheng *et al.*[18] have got around $8\text{-}10 \text{ cm}^{-1}$ difference between experiment and theory even after including spin-orbit interactions. For Bi_2Te_3 film, the frequencies of most of the modes match nicely with the experimental observations except for the highest mode which is overestimated and can be lowered with the incorporation of spin-orbit interactions.[18] The band structure of Bi_2Te_3 film is resolved correctly when including spin-orbit effect and the Dirac cone is observed at the Γ point in the Brilluon zone and is illustrated in Fig. S3 in supplementary. The errors in mode frequencies in DFT are due to the sensitivity of calculation with the external stresses which is seen in previous calculations.

Conclusions

A comprehensive study of temperature dependent Raman spectra in layered single crystals of $\text{Pb}_2\text{Bi}_2\text{Te}_3$, PbBi_2Te_4 and PbBi_4Te_7 has been presented. The general blue shift trends with decrease in temperature are observed for all studied materials due to their similar lattice structures. The overall agreement between theoretically calculated DFT and experimentally observed modes at 93 K is quite good for all the samples. In the phonon density of states, Pb atoms contribute mainly in the lower frequency region whereas higher frequency contribution comes from Te and Bi. We found that at temperatures above 150 K, the frequency of the A_{1g}^2 phonon change linearly with temperature. Whereas below 150 K the evaluation of A_{1g}^2 modes are best fitted by nonlinear polynomial and are understood by the inclusion

of anharmonic phonon-phonon coupling for $\text{Pb}_2\text{Bi}_2\text{Te}_3$. Analogous electronic, crystal structure and Raman spectra of $\text{Pb}_2\text{Bi}_2\text{Te}_3$ and Bi_4Te_3 indicate that $\text{Pb}_2\text{Bi}_2\text{Te}_3$ may be a promising candidate of topological semimetal, though the ARPES measurement is necessary to confirm the topological property in $\text{Pb}_2\text{Bi}_2\text{Te}_3$. The experimentally observed Raman modes for PbBi_2Te_4 and PbBi_4Te_7 at the same frequencies as that of Bi_2Te_3 explain theoretically under the harmonic approximations by lattice thermal expansion and enhancement of interaction stiffness affects. The insertion of Pb and PbTe layers in Bi_2Te_3 introduces chemical pressure in the unit cell of Bi_2Te_3 and modifies the interactions at the QLS boundary results in observation of A_{1u}^2 mode. Furthermore at the lowest measured temperature, the A_{1u}^1 mode becomes the highest one reflects the enhancement of the out-of-plane Bi-Te vibrations relative to the in-plane Bi-Te vibrations. Similar observation is made for structural evolution of Bi_2Te_3 to PbBi_4Te_7 .

ACKNOWLEDGEMENTS

Pradip Das and Priyanath Mal acknowledge the Department of Science and Technology for financial support through project no. SR/FTP/PS-197/2012. Authors of GGV also thank to UGC, Govt. of India for supporting the Department of Pure and Applied Physics through UGC SAP DRS –I and FIST Level – I programs respectively. Brahmananda Chakraborty would like to thank Dr. N. K. Sahoo for support and encouragement. Brahmananda Chakraborty would also like to thank the staff of BARC computer division for supercomputing facility.

[†]pradipd.iitb@gmail.com

^{*}brahma@barc.gov.in

References

- 1 M. Z. Hasan and C. L. Kane, *Rev. Mod. Phys.* **82**, 3045-3067 (2010).
- 2 X. -L. Qi and S. -C. Zhang, *Rev. Mod. Phys.* **83**, 1057-1110 (2011).
- 3 J. E. Moore, *Nature (London)* **464**, 194 (2010).
- 4 M. S. König, C. Wiedmann, A. Brüne, H. Roth and L. Buhmann, *Science* **318**, 766 (2007).
- 5 D. Pesin and A. H. MacDonald, *Nature Mater.* **11**, 409 (2012).
- 6 D. A. Wright, *Nature* **181**, 834 (1958).
- 7 M. Saleemi, M. S. Toprak, S. Li, M. Johnssonb and M. Muhammed, *J. Mater. Chem.* **22**, 725 (2012).
- 8 L. Zhang and D. J. Singh, *Phys. Rev. B* **81**, 245119 (2010).
- 9 T. V. Quang and M. Kim, *Journal of the Korean Physical Society* **68**, 393 (2016).
- 10 J. J. Zhou, W. Feng, Y. Zhang, S. A. Yang and Y. Yao, *Sci. Rep.* **4**, 3841 (2014).
- 11 S. Barua, K. P. Rajeev and A. K. Gupta, *J. Phys.: Condens. Matter* **27**, 015601 (2015).
- 12 K. Kuroda, H. Miyahara, M. Ye, S. V. Eremeev, Yu. M. Koroteev, E. E. Krasovskii, E. V. Chulkov, S. Hiramoto, C. Moriyoshi, Y. Kuroiwa, K. Miyamoto, T. Okuda, M. Arita, K. Shimada, H. Namatame, M. Taniguchi, Y. Ueda and A. Kimura, *Phys. Rev. Lett.* **108**, 206803 (2012).
- 13 T. Okuda, T. Maegawa, M. Ye, K. Shirai, T. Warashina, K. Miyamoto, K. Kuroda, M. Arita, Z. S. Aliev, I. R. Amiraslanov, M. B. Babanly, E. V. Chulkov, S. V. Eremeev, A. Kimura, H. Namatame and M. Taniguchi, *Phys. Rev. Lett.* **111**, 206803 (2013).

- 14 C. Wang, X. Zhu, L. Nilsson, J. Wen, G. Wang, X. Shan, Q. Zhang, S. Zhang, J. Jia and Q. Xue, *Nano Res.* **6**, 688 (2013).
- 15 V. Chis, I. Yu. Sklyadneva, K. A.Kokh, V. A. Volodin and O. E. Tereshchenko and E. V. Chulkov, *Phys. Rev. B* **86**, 174304 (2012).
- 16 K. M. F. Shahil, M. Z. Hossain, V. Goyal and A. A. Balandin, *J. Appl. Phys.* **111**, 054305 (2012).
- 17 J. Yuan, M. Zhao, W. Yu, Y. Lu, C. Chen, M. Xu, S. Li, K. P. Loh and Q. Bao, *Materials* **8**, 5007 (2015).
- 18 W. Cheng and S. F. Ren, *Phys. Rev. B* **83**, 094301 (2011).
- 19 T. Hirahara, G. Bihlmayer, Y. Sakamoto, M. Yamada, H. Miyazaki, S. Kimura, S. Blugel and S. Hasegawa, *Phys. Rev. Lett.* **107**, 166801 (2011).
- 20 H. Xu, Y. Song, W. Pan, Q. Chen, X. Wu, P. Lu, Q. Gong and S. Wang, *AIP Advances* **5**, 087103 (2015).
- 21 J. W. G. Bos, H. W. Zandbergen, M. -H. Lee, N. P. Ong and R. J. Cava, *Phys. Rev. B* **75**, 195203 (2007).
- 22 H. Lind, S. Lidin and U. Häussermann, *Phys. Rev. B* **72**, 184101 (2005).
- 23 T. Valla, H. Ji, L. M. Schoop, A. P. Weber, Z. -H. Pan, J. T. Sadowski, E. Vescovo, A. V. Fedorov, A. N. Caruso, Q. D. Gibson, L. Müchler, C. Felser and R. J. Cava, *Phys. Rev. B* **86**, 241101(R) (2012).
- 24 V. Russo, A. Bailini, M. Zamboni, M. Passoni, C. Conti, C. S. Casari, A. L. Bassi and C. E. Bottani, *J. Raman Spectrosc.* **39**, 205 (2008).
- 25 J. Rodríguez-Carvajal, *An introduction to the program France: FullProf 2000; 2001*
- 26 K. Momma and F. Izumi, *J. Appl. Crystallogr.* **44**, 1272 (2011).
- 27 D. Teweldebrhan, V. Goyal and A. A. Balandin, *Nano Lett.* **10**, 1209 (2010).

- 28 D. Park, S. Park, K. Jeong, H. –S. Jeong, J. Y. Song and M. –H. Cho, Sci. Rep. **6**, 19132 (2016).
- 29 R. He, Z. Wang, R. L. J. Qiu, C. Delaney, B. Beck, T. E. Kidd, C. C. Chancey and X. P. A. Gao, Nanotechnology **23**, 455703 (2012).
- 30 G. J. -Hua, Q. Feng, Z. Yun, D. H. -Yong, H. G. -Jin, L. X. -Nan, Y. G. -Lin and D. Ning, Chin. Phys. Lett. **30**, 106801 (2013).
- 31 C. R. -Fernández, C. V. Manzano, A. H. Romero, J. Martín, M. M. -González, M. M. de Lima Jr and A. Cantarero, Nanotechnology **27**, 075706 (2016).
- 32 Y. Kim, X. Chen, Z. Wang, J. Shi, I. Miotkowski, Y. P. Chen, P. A. Sharma, A. L. L. Sharma, M. A. Hekmaty, Z. Jiang and D. Smirnov, Appl. Phys. Lett. **100**, 071907 (2012).
- 33 M. S. Liu, L. A. Bursill, S. Praver and R. Beserman, Phys. Rev. B **61**, 3391 (2000).
- 34 P. Giannozzi, S. Baroni, N. Bonini, M. Calandra, R. Car, C. Cavazzoni, D. Ceresoli, G. L. Chiarotti, M. Cococcioni, I. Dabo, A. D. Corso, S. Fabris, G. Fratesi, S. de Gironcoli, R. Gebauer, U. Gerstmann, C. Gougoussis, A. Kokalj, M. Lazzeri, L. M. -Samos, N. Marzari, F. Mauri, R. Mazzarello, S. Paolini, A. Pasquarello, L. Paulatto, C. Sbraccia, S. Scandolo, G. Sclauzero, A. P. Seitsonen, A. Smogunov, P. Umari, R. M. Wentzcovitch, J. Phys.: Condens. Matter. **21**, 395502 (2009).
- 35 <http://theosrv1.epfl.ch/Main/Pseudopotentials>
- 36 H. J. Monkhorst and J. D. Pack, Phys. Rev. B **13**, 5188 (1976).
- 37 A. Togo and I. Tanaka, Scr. Mater. **108**, 1 (2015).

Figure captions

Figure 1: (a) Red, black and blue solid lines are observed, calculated and difference pattern profiles respectively, obtained from the refinement of the room temperature powder diffraction data. The green vertical parallel ticks above the difference profile correspond to the Bragg peak position. (b) X-ray diffraction of the mechanically exfoliated single crystalline planes. All the peaks observed in the recorded pattern are indexed according to the growth direction. The single crystalline plane of $\text{Pb}_2\text{Bi}_2\text{Te}_3$ and optical image of the crystalline plane for PbBi_2Te_4 are illustrated in the inset (second and third row).

Figure 2: Schematic representation of unit cells of (a) Bi_2Te_3 , (b) $\text{Pb}_2\text{Bi}_2\text{Te}_3$, (c) PbBi_2Te_4 and (d) PbBi_4Te_7 respectively, looking along crystallographic a axis: the solid line represents the unit cell. The bond lengths are in Å.

Figure 3: Temperature dependent Raman spectra of (a) $135\ \mu\text{m}$ Bi_2Te_3 , (b) $61\ \mu\text{m}$ $\text{Pb}_2\text{Bi}_2\text{Te}_3$, (c) $151\ \mu\text{m}$ PbBi_2Te_4 and (d) $104\ \mu\text{m}$ PbBi_4Te_7 are recorded with 532 nm laser diode source with a spectral resolution of $1\ \text{cm}^{-1}$. The Lorentzian line shape fitting of the RT and 93 K modes are illustrated in the main panel and inset respectively. Blue lines correspond to individual peak fit and that of red lines represents the peak sum.

Figure 4: Mode shift and full width half maxima (FWHM) variations with temperature for (a) Bi_2Te_3 , (b) $\text{Pb}_2\text{Bi}_2\text{Te}_3$, (c) PbBi_2Te_4 and (d) PbBi_4Te_7 . Black, red and green colored axes correspond to Temperature, FWHM and Raman shift respectively. Red open circles and green open square represents FWHM and peak position respectively. Dashed black and blue lines represent the linear fit and quadratic fit of anharmonic phonon-phonon coupling respectively.

Figure 5: Total density of states of (a) $\text{Pb}_2\text{Bi}_2\text{Te}_3$, (b) PbBi_2Te_4 and (c) PbBi_4Te_7 respectively. The dashed black line corresponds to the Fermi level.

Figure 6: Partial phonon density of states of (a) $\text{Pb}_2\text{Bi}_2\text{Te}_3$, (b) PbBi_2Te_4 and (c) PbBi_4Te_7 respectively.

Table captions

Table 1: Comparison of first order temperature coefficient (χ') of different Raman modes of Bi_2Te_3 , $\text{Pb}_2\text{Bi}_2\text{Te}_3$, PbBi_2Te_4 and PbBi_4Te_7 .

Table 2: The characteristics Raman frequencies of different specimens calculated theoretically and experimentally observed at 93 K.

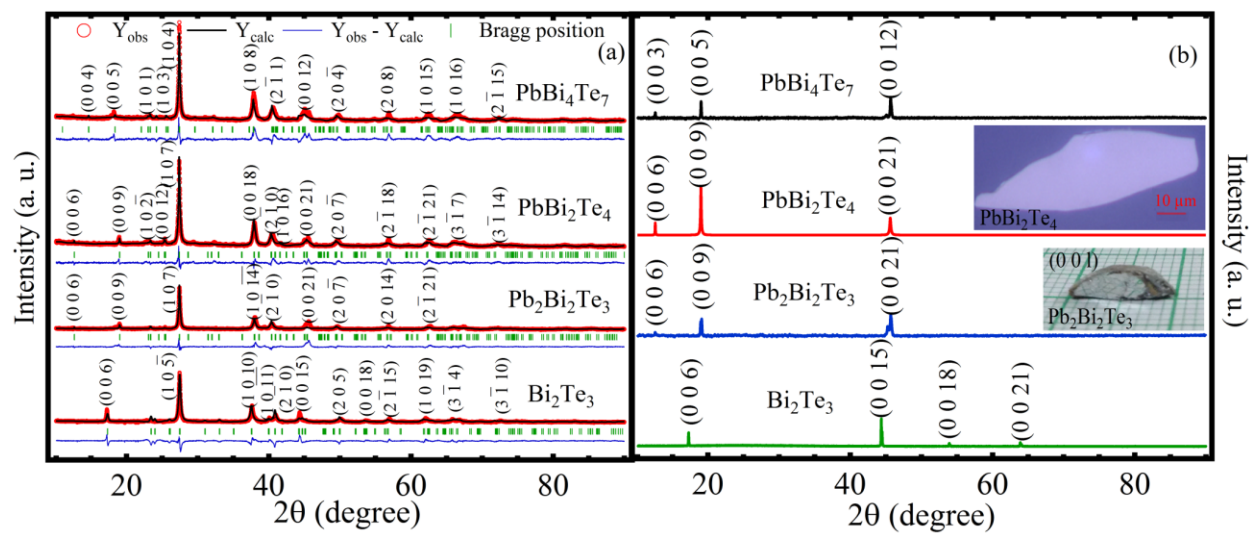


Figure 1

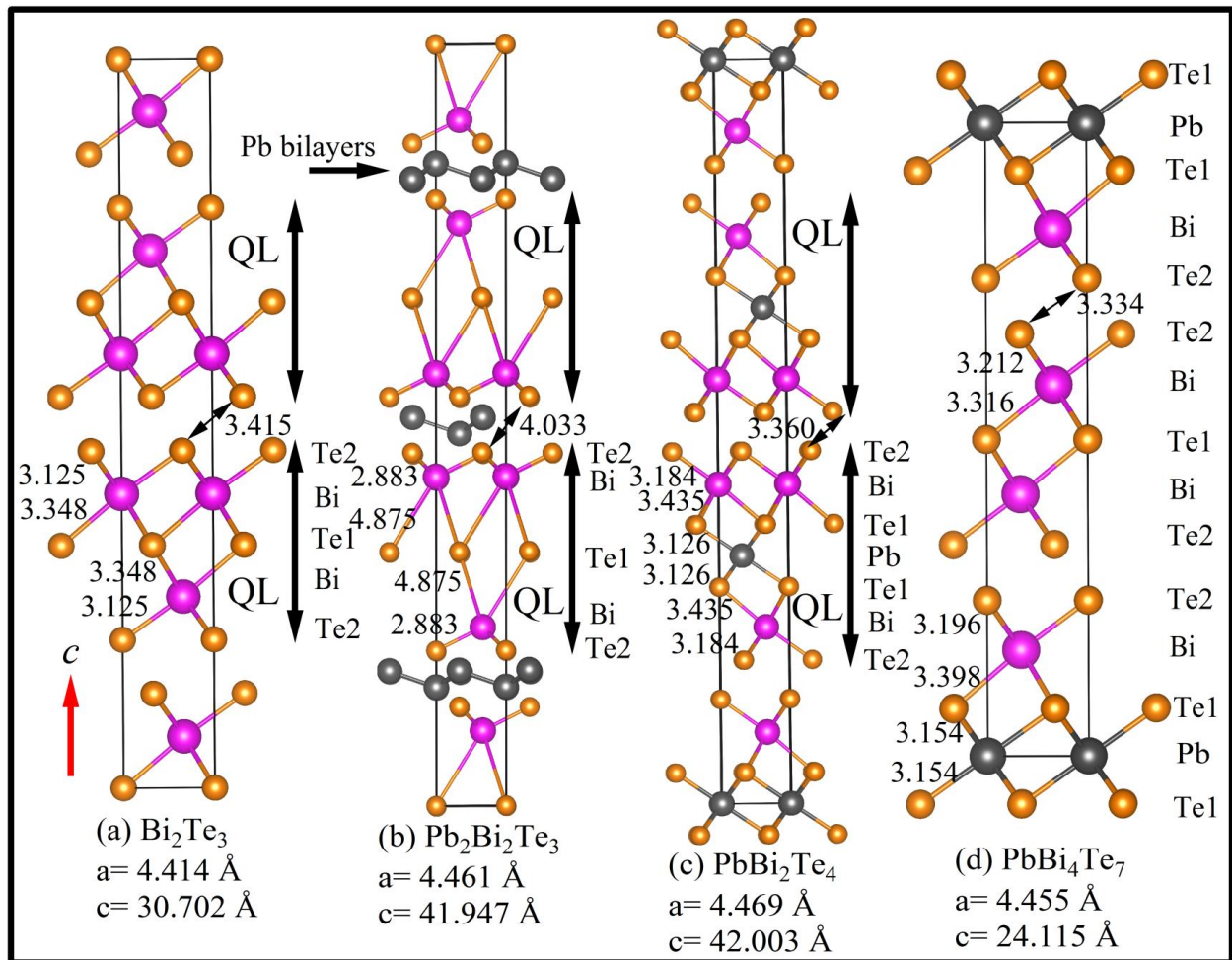


Figure 2

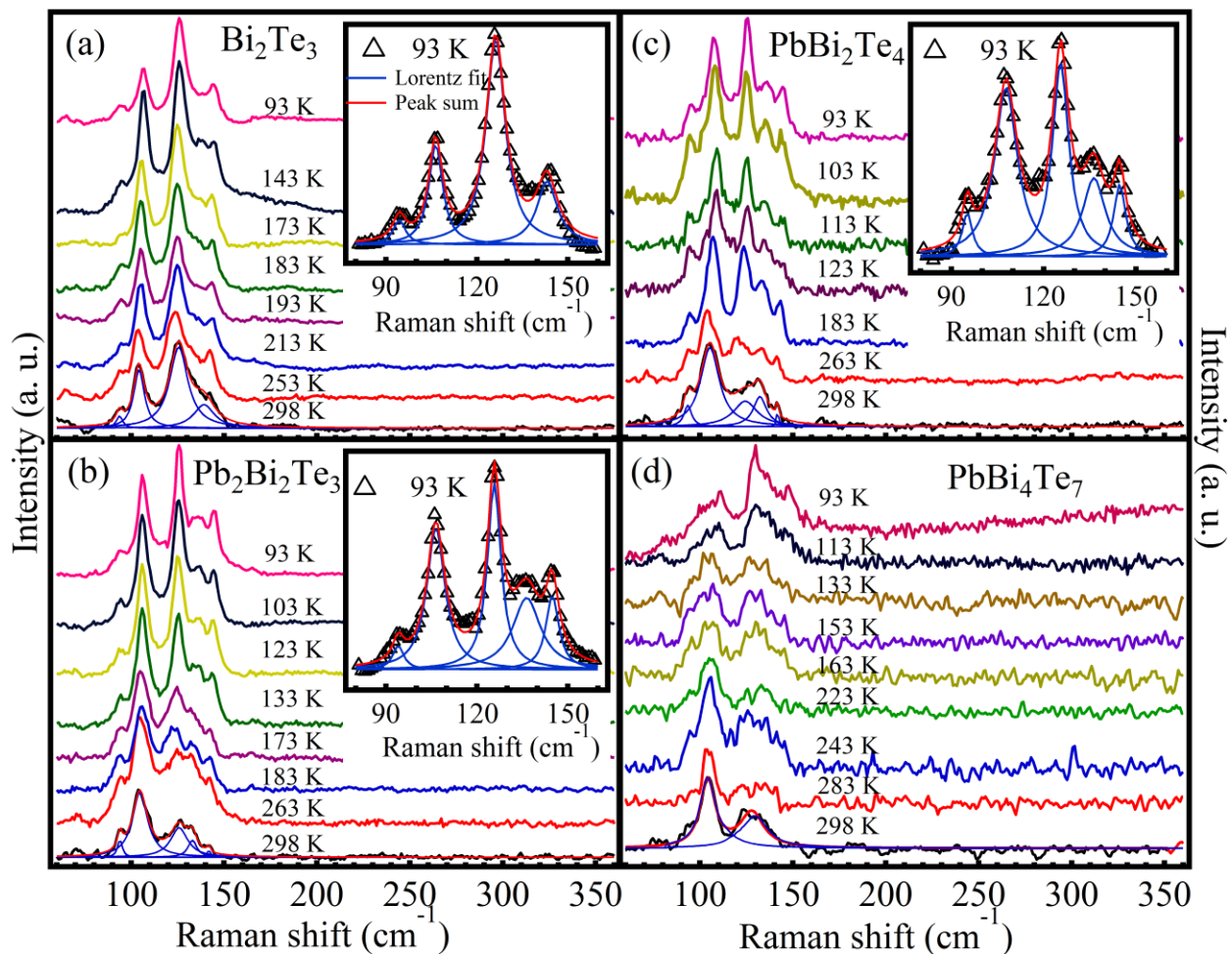


Figure 3

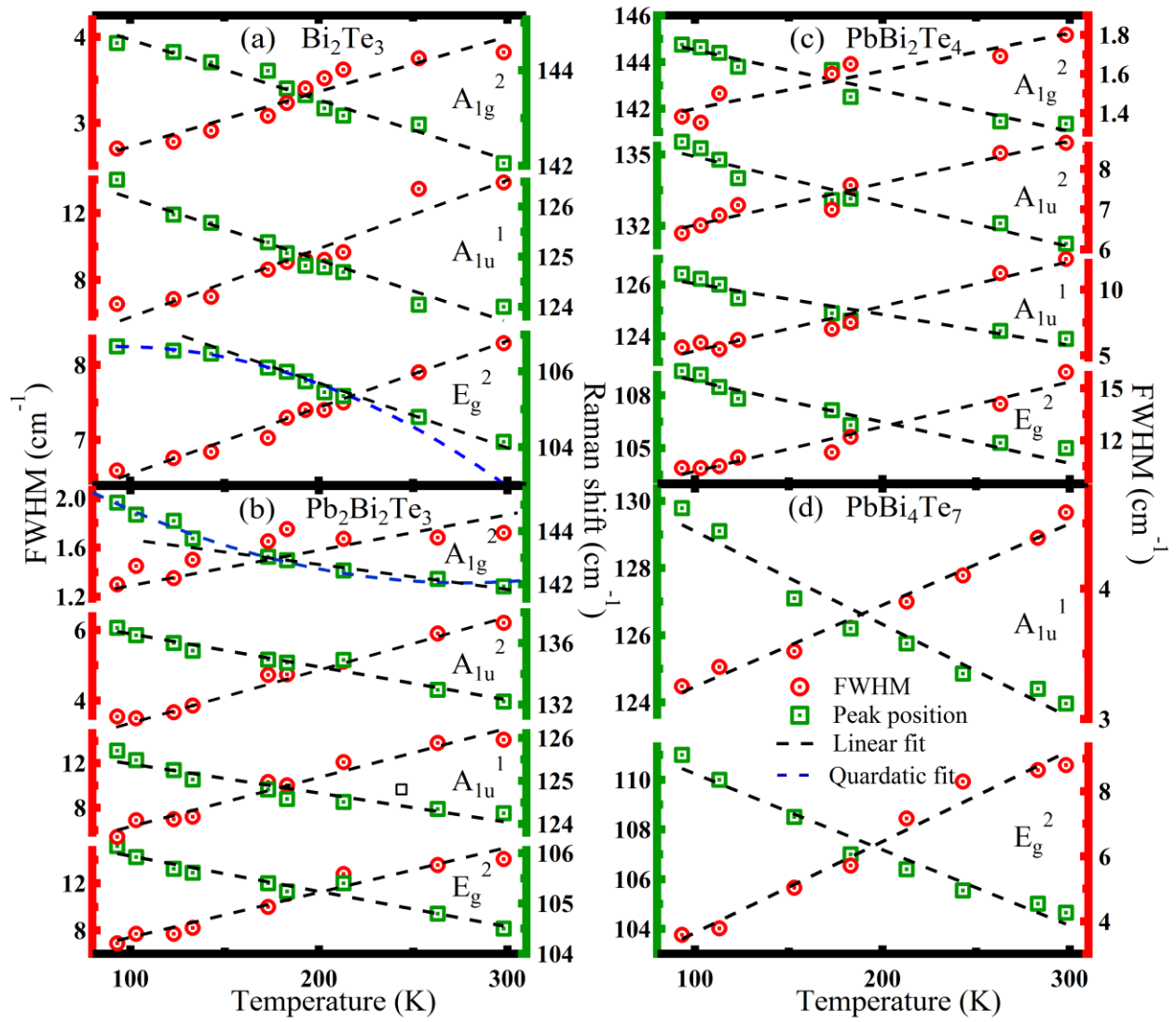


Figure 4

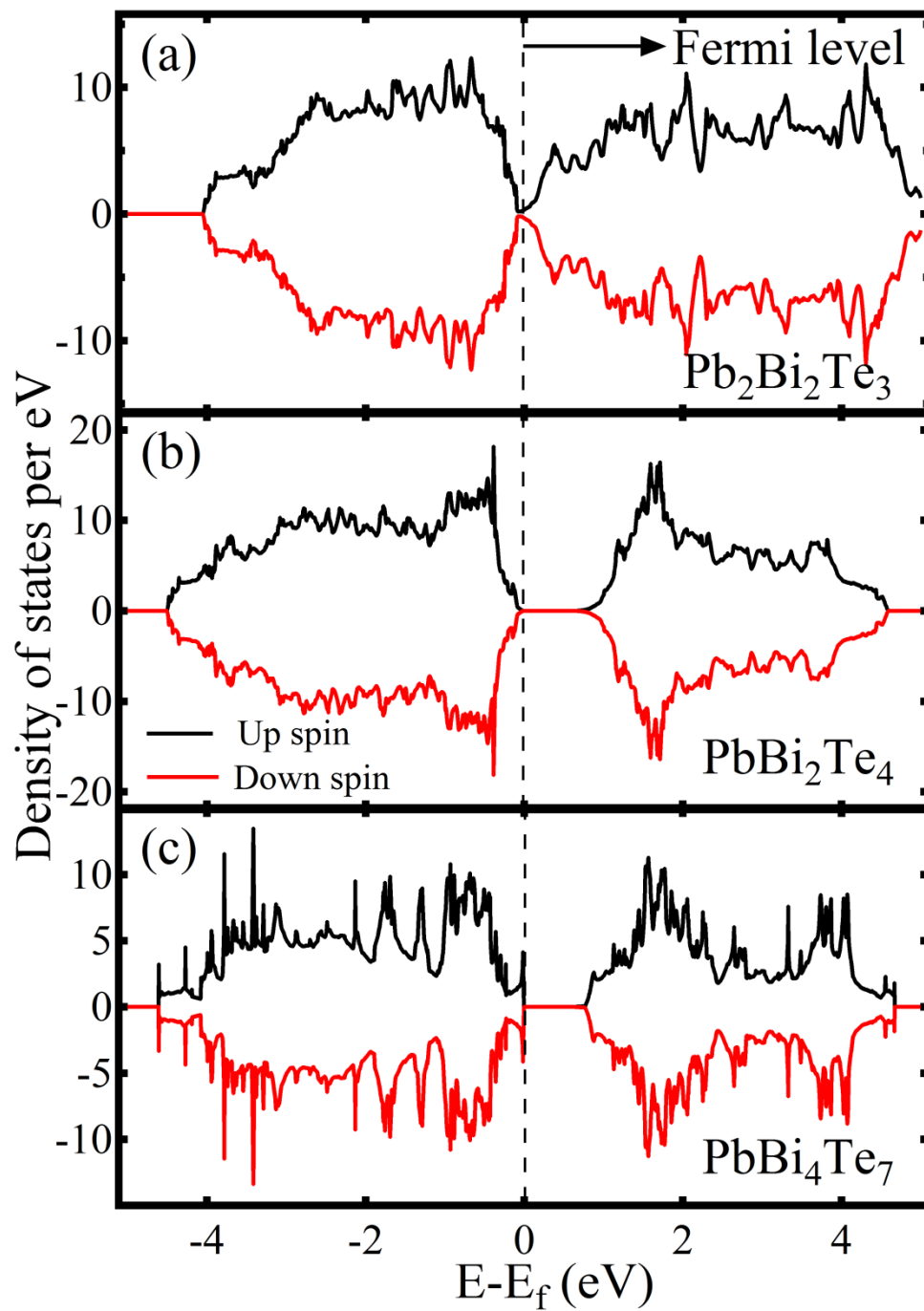


Figure 5

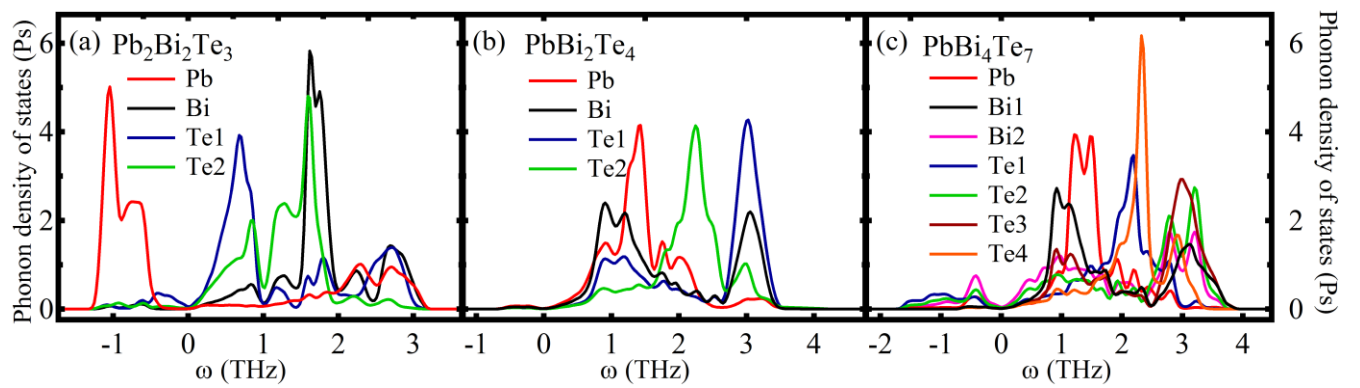


Figure 6

Table 1

Sample name	Raman modes	χ' : slope of linear fit ($\text{cm}^{-1}\text{K}^{-1}$)
Bi_2Te_3	E_g^2	-0.01317 ± 0.00094
	A_{1u}^1	-0.01252 ± 0.00119
	A_{1g}^2	-0.01264 ± 0.00083
$\text{Pb}_2\text{Bi}_2\text{Te}_3$	E_g^2	-0.00704 ± 0.00065
	A_{1u}^1	-0.00678 ± 0.00089
	A_{1u}^2	-0.00568 ± 0.00029
	A_{1g}^2	-0.00869 ± 0.00072
PbBi_2Te_4	E_g^2	-0.02331 ± 0.00192
	A_{1u}^1	-0.01195 ± 0.00153
	A_{1u}^2	-0.01748 ± 0.00177
	A_{1g}^2	-0.01933 ± 0.00196
PbBi_4Te_7	E_g^2	-0.03051 ± 0.00244
	A_{1u}^2	-0.02771 ± 0.00242

Table 2

Bi ₂ Te ₃ Mode frequency (cm ⁻¹)		Pb ₂ Bi ₂ Te ₃ Mode frequency (cm ⁻¹)		PbBi ₂ Te ₄ Mode frequency (cm ⁻¹)		PbBi ₄ Te ₇ Mode frequency (cm ⁻¹)	
Theo.	Expt.	Theo.	Expt.	Theo.	Expt.	Theo.	Expt.
27	-----	-----	-----	-----	-----	-----	-----
-----	94	94	94	81	95	91	-----
101	~107	102	106	105	107	105	111
123	~127	-----	~126	111	~127	122	~130
-----	-----	-----	137	114	~136	128	-----
158	~145	-----	145	-----	~145	-----	147

Supplementary information

Figure S1: Thickness of (a) Bi_2Te_3 , (b) $\text{Pb}_2\text{Bi}_2\text{Te}_3$, (c) PbBi_2Te_4 and (d) PbBi_4Te_7 single crystal flakes measured through optical microscope.

Figure S2: EDAX spectra for (a) Bi_2Te_3 , (b) $\text{Pb}_2\text{Bi}_2\text{Te}_3$, (c) PbBi_2Te_4 and (d) PbBi_4Te_7 single crystal flakes.

Figure S3: Band structure of Bi_2Te_3 .

Figure S4: Phonon dispersion of Bi_2Te_3 .

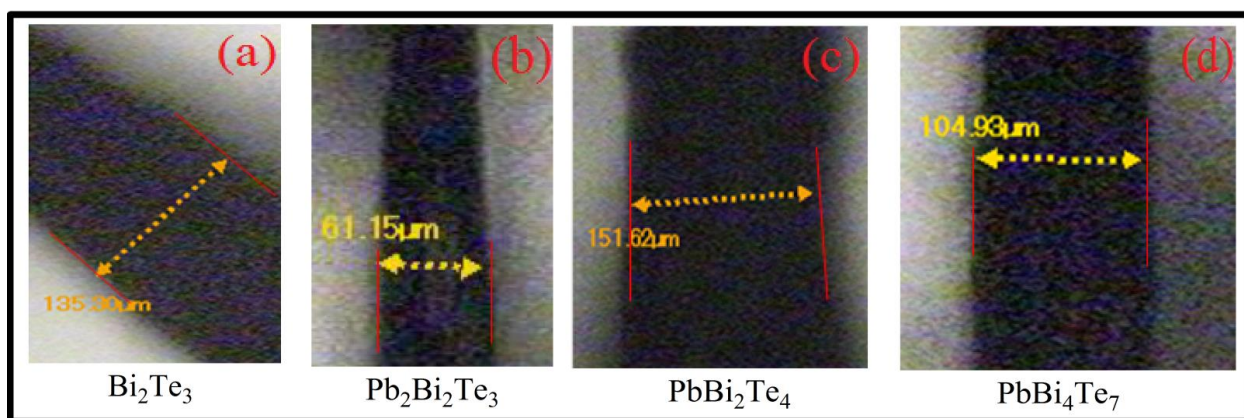
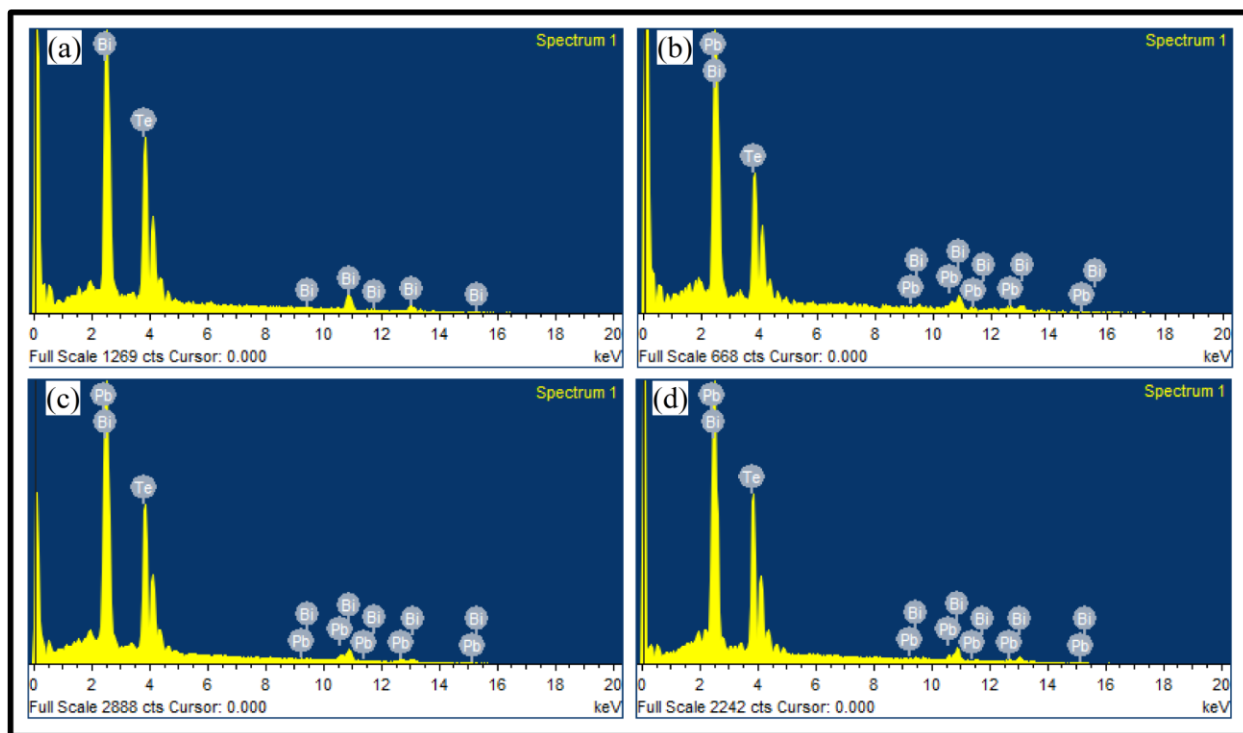


Figure S1



Specimen	Weight (%)	
	Theoretical	Experimental
Bi_2Te_3	Bi: 52.19	Bi: 52.24
	Te: 47.80	Te: 47.47
$\text{Pb}_2\text{Bi}_2\text{Te}_3$	Pb: 34.0	Pb: 32.83
	Bi: 34.40	Bi: 33.43
	Te: 31.50	Te: 33.74
PbBi_2Te_4	Pb: 19.31	Pb: 19.31
	Bi: 36.57	Bi: 35.73
	Te: 45.11	Te: 44.96
PbBi_4Te_7	Pb: 10.70	Pb: 10.10
	Bi: 43.17	Bi: 43.16
	Te: 46.12	Te: 46.73

Figure S2

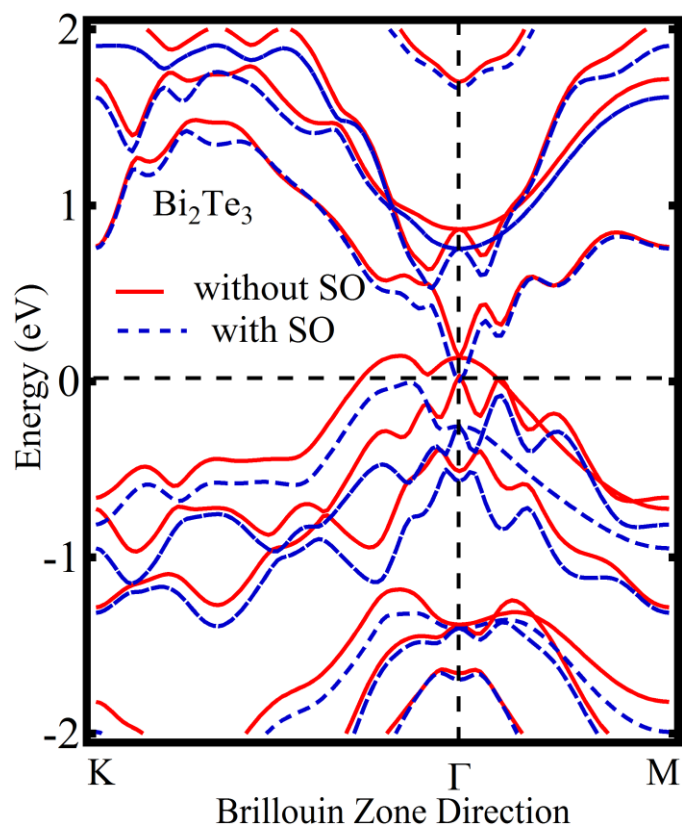


Figure S3

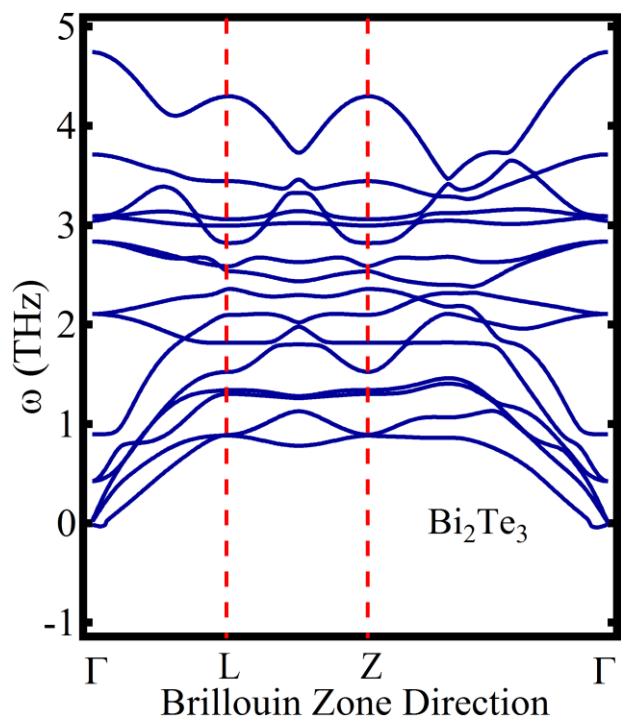


Figure S4